Colloid and Polymer Science (2019) 297:1365–1373
https://doi.org/10.1007/s00396-019-04555-w

ORIGINAL CONTRIBUTION

Pore connectivity effects on the internal surface electric charge of mesoporous silica

Tumcan Sen[1] · Murat Barisik[1]

Received: 20 April 2019 / Revised: 7 July 2019 / Accepted: 11 August 2019 / Published online: 11 September 2019

Abstract

Nano-scale confinements within mesoporous systems develop overlapping electric double layers (EDL) such that the existing theoretical models cannot predict the electric potential distributions and resulting surface charges. In addition, ionic conditions undergo local variation through connections between the pore voids and pore throats. For the first time in literature, we studied the charging behavior of mesoporous silica in terms of the pore to throat size ratio (R_{pt}) to characterize the pore connectivity effects, in addition to porosity (ϵ) and pore size (H). Both local and average surface charge densities inside mesoporous silica were examined by varying these parameters systematically. Results showed that the magnitude of surface charge density decreased with increasing EDL overlap and decreasing connectivity effects. We formulized this behavior and developed an extended model to predict mesoporous silica's internal charge as a function of porosity, pore size, and pore to throat size ratio.

Keywords Mesoporous silica · Internal surface electric charge · Poisson-Nernst-Planck equations · Charge regulation model · Porosity · Pore to throat connectivity

Nomenclature

EDL	Electric double layer
BD	Boltzmann distribution
PNP	Poisson-Nernst-Planck
CR	Charge regulation
REV	Representative elementary volume
H	Pore size
R_{pt}	Pore to throat size ratio
c_{10}	Bulk concentration of H^+
c_{20}	Bulk concentration of K^+
c_{30}	Bulk concentration of Cl^-
c_{40}	Bulk concentration of OH^-
ε	Porosity
λ	Debye length
κ	Debye-Hückel parameter
ε_0	Permitivity of vacuum
ε_r	Dielectric constant
k_B	Boltzmann constant
T	Temperature
N_A	Avagadro constant
e	Elementary charge
c_i	Local concentration of the ith ion
z_i	Valance of the ith ion
Ψ	Electric potential
N_i	Flux density
D	Diffusivity
F	Faraday constant
R	Universal gas constant
Γ	Site density
K_A, K_B	Equilibrium constants
σ	Surface charge density
AR	Aspect ratio of the solid parts

✉ Murat Barisik
muratbarisik@iyte.edu.tr

[1] Department of Mechanical Engineering, Izmir Institute of Technology, 35430 Izmir, Turkey

Ordered mesoporous silica–based materials have been synthesized in various morphologies since their development in the early 1990s. This generated a diverse range of interest in these materials across several fields due to their uniquely ordered pore structures, high surface area and pore volume, tunable/uniform pore sizes, chemical stability, and bio-compatibility characteristics. Recent applications such as targeted drug delivery [1, 2], gated/functionalized sensing [3, 4], organic/inorganic nano-filtration [5], energy production/conversion/storage [6, 7], and pollutant removal via adsorbent [8, 9] systems are utilizing mesoporous structures. In the operation of

these applications, surface charge density resulting from the silanol groups on the silica surface plays a crucial role. Yet, a comprehensive understanding of the behavior of surface charge density within the mesoporous structures in terms of pore structural parameters such as pore size, porosity, and pore connectivity is still lacking.

Interaction between the ions within the electrolyte solutions and silanol groups on the silica surfaces yields a net electric charge on the surface. As the interconnected pore structures of mesoporous materials allow the ions to diffuse into the pores, both outer and inner surfaces develop surface charge as a function of the ionic environment. While the outer surface charge has been widely studied, internal surface charge has been mostly overlooked in the current literature. Outer surface charge can easily be calculated as a function of local ionic properties. However, inner charge deviates from these classical calculations largely due to electric double layer (EDL) overlaps developing in nano-scale confinements. There are some experimental studies dedicated to determining internal surface charge based on the streaming potential [10–14] or potentiometric titration [15–19]. However, only a few of these studies focus on influences of porous system parameters but do not explain or correlate the physical mechanism behind the internal surface charging [20, 21]. There are also theoretical studies evaluating overall charging behavior of porous structures based on the site dissociation models [10, 11, 22]. However, many of those studies assume that the ionic distribution within the EDL obeys Boltzmann distribution (BD), which is not applicable for overlapped EDLs of mesoporous systems. When the size of nano-scale confinement is comparable with the thickness of the EDL, ionic layers (EDLs) growing from opposite surfaces overlap that ionic distribution over the surface becomes different than Boltzmann distribution. Hence, implementing the Boltzmann distribution to the Poisson equation becomes incorrect [23, 24]. Instead, Nernst-Planck equation should be coupled with the Poisson equation (i.e., Poisson-Nernst-Planck (PNP) equations) to calculate the electric potential and ionic distributions. There are numerical studies solving PNP equations for simpler geometries such as single nano-pores or slit nano-channels [25–29]. Specifically, overlap effects are taken into account by active charge models called charge regulation (CR) [30]. In this context, we recently employed the PNP equations along with the CR model and presented deviation of inner surface charge from flat surface theory predictions also with a strong local variation through the reservoir connections of short nano-channels [31]. We further extended our study on mesoporous systems and systematically examined the inner surface charging showing local variations due to (i) overlap of EDLs extending from opposite surfaces in the pore throats and (ii) connectivity effects between the ionic conditions of pore throat and pore void [32]. Ultimately, an overall charging behavior is presented in terms of porosity and pore size.

In general, porous systems are characterized by porosity and pore size. However, such characterization is incomplete. In a porous system, the pore network is formed in such a way that pore voids are connected to each other through channels, also called pore throats. The structure of a porous medium is defined by how these throats connect the neighboring pores to each other. The internal network of two porous systems can be completely different even if they have identical porosity and pore size values. This structural difference results in various ionic and potential distributions inside mesoporous mediums depending on their pore connections. Hence, the ratio of pore throat size to pore size becomes an important parameter, which should be considered for a correct characterization of pore network [33–37] and corresponding charging behavior.

The objective of the current study is to demonstrate that the relative size of pore throat to pore body (i.e., pore connectivity) also plays a crucial role on charge density in addition to the commonly studied structural parameters such as porosity and pore size. For the first time in literature, the pore to throat size ratio concept is applied to resolve surface charge characteristics inside mesoporous silica. Local properties of ionic distribution and surface charge are evaluated by multi-ion-charge regulation model [38, 39]. We aim to extend our earlier phenomenological model [32] to include connectivity effects, in addition to porosity and pore size. CR boundary condition is implemented on the charged surfaces to mimic the physical response of the surface chemistry. This model takes into account the protonation/deprotonation reactions on the interface resulting from interaction silanol groups with dissolved ions in the electrolyte solution as a function of pH and salt concentration. The Poisson-Nernst-Planck equations are employed to model the electrostatic behavior and diffusion of ions inside mesoporous silica.

Mathematical and numerical model

Various forms and sizes of mesoporous systems have been synthesized by multiple research groups. Specifically, MCM (Mobil Composition of Matter) [40, 41], KIT (Korea Institute of Technology) [42, 43], SBA (Santa Barbara Amorphous) [44, 45], and FDU (Fudan University in Shanghai) [46] highly ordered mesoporous silicates with a rich variety and precise control over shape and size. Varying synthesis conditions yield various forms of mesoporous silica distinguishable by a number and a space group. MCM-41 (hexagonal), MCM-48 (cubic), MCM-50 (lamellar), KIT-5 (cubic cage structures), KIT-6 (cubic), SBA-1 (cubic), SBA-11 (cubic), SBA-12 (3D hexagonal network), SBA-14 (lamellar), SBA-15 (2D hexagonal), SBA-16 (cubic cage structured), FDU-1 (cubic), and FDU-12 (cubic) are examples with the very well-ordered arrangements of porous voids and connecting throats of different geometries. Recently, cubic silicates with highly ordered

periodic structures repeating in either two- or three-dimension received the most attention due to their easily tunable porous network parameters such as pore and throat size. Multiple studies synthesized high-quality cubic mesoporous materials with a desired structure. For instance, ordered periodic pore arrays of SBA-16 can easily be controlled such that desired pore diameter and pore throat size can be obtained by the synthesis temperature and time [47]. We draw a simple unit cell description of SBA-16 (Im3m) in Fig. 1a similar to the experimentally determined structure by electron crystallography [48] and also similar to earlier studies [49–52]. In this study, we simplified such three-dimensional structure into a two-dimensional representation due to computational cost.

The two-dimensional representative volume (REV) is shown in Fig. 1b. This REV illustrates four-unit cells of mesoporous silica with highly ordered three-dimensional close-packed, cage-like structure. While the pore size is indicated by H, the porosity is defined as the ratio of non-solid volume to pore volume. An additional structural parameter, R_{pt}, is also introduced which is the ratio of pore throat size to pore size. The variation of pore throat size described in Kim et al. [47] was illustrated in Fig. 1a in SBA-16 synthesis. This parameter changes the layout of the porous media even if porosity is kept constant. In this study, simulations are performed for changing porosities (ϵ), pore sizes (H), and pore size to throat size ratios (R_{pt}). Simply, porosity was altered by changing the area of the solid parts while the size of solid parts determined the pore throat size. Variation of pore throat size at a given pore size (H) and porosity is illustrated in Fig. 2. Porous system parameters are varied systematically while keeping the minimum confinement size above 4 nm so that molecular interactions can be safely neglected.

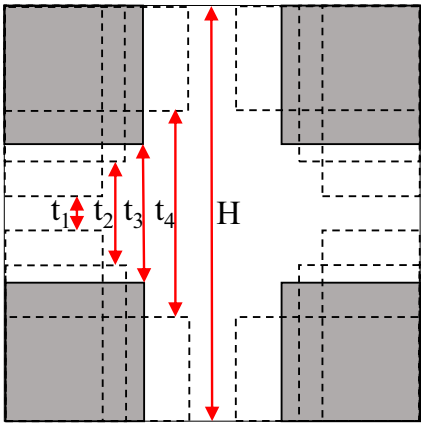

Fig. 2 Illustration of throat size (t) variation at a given constant pore size (H) and porosity

The electrolyte is a symmetric KCl solution and contains H^+, K^+, Cl^-, and OH^- ions with the ith specie's bulk molar concentration and valance being c_i and z_i ($i = 1$ for H^+; $i = 2$ for K^+; $i = 3$ for Cl^-; $i = 4$ for OH^-). Bulk concentrations of these species are chosen so that the electroneutrality condition is satisfied. Hence, $c_{10} = 10^{-pH+3}$, $c_{40} = 10^{-(14-pH)+3}$, $c_{20} = c_{KCl}$, and $c_{30} = c_{KCl} + c_{10} - c_{40}$ for pH < 7; $c_{20} = c_{KCl} + c_{10} - c_{40}$ and $c_{30} = c_{KCl}$ for pH > 7. Debye length that characterizes the electric double layer can be calculated as $\lambda = {}^{1}/_{\kappa} = \sqrt{\varepsilon_0 \varepsilon_r k_B T / N_A e^2 \sum c_i z_i^2}$ where ε_0 and ε_r are the permittivity of vacuum and dielectric constant of the electrolyte, respectively. The variation of dielectric constant as a function of potential gradient normal to solid surface is neglected since this variation is not significant compared with other effecting parameters in the system [54]. Boltzmann and Avogadro constants are denoted by k_B and N_A, respectively, while T is the

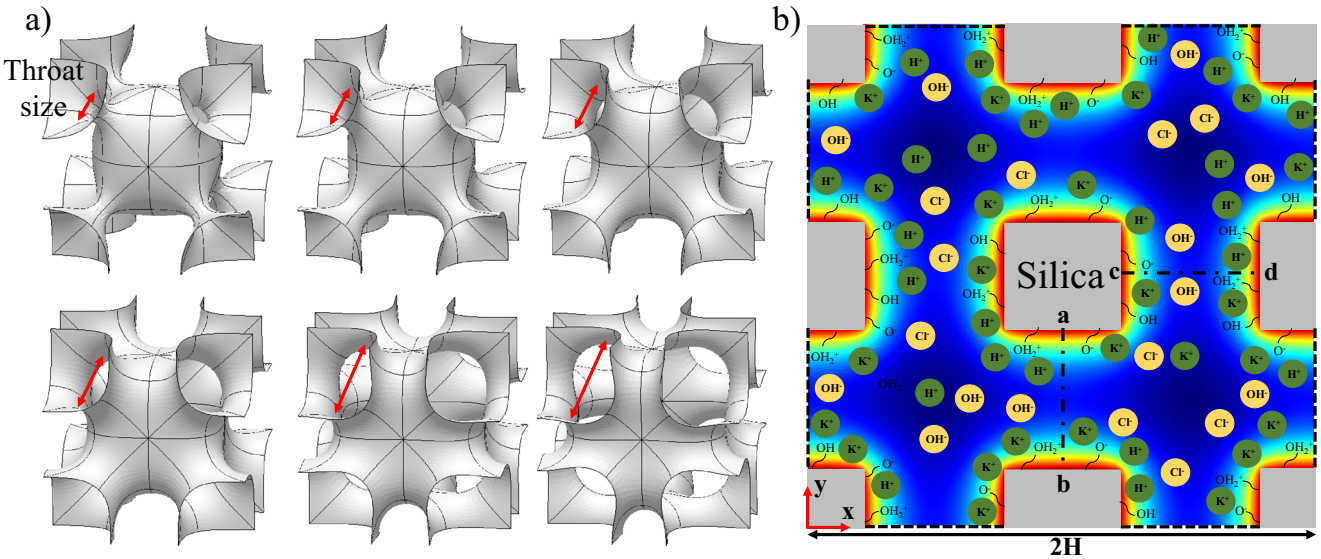

Fig. 1 **a** Three-dimensional cubic cage structure of SBA-16 (Im3m) [49–52] at various throat sizes [47]. Structures developed by using Surface Evolver [53]. **b** Schematic illustration of the representative elementary volume for four-unit cells. Here H is the pore size and ab and cd lines denote the cross sections whose electric potential and ionic distributions are used in the iteration procedure

temperature and e is the elementary charge. Electrostatic potential and the ion flux are governed by Poisson-Nernst-Plank (PNP) equations presented in Eqs. (1) and (2). PNP model as is neglects the ion size effects and dispersion forces by treating the ions as point charges [55]. In Eqs. (1) and (2), ψ is the electric potential, $\overrightarrow{N}_i$ is the flux density, D_i is the diffusivity, and F and R are the Faraday and the universal gas constants, respectively.

$$-\varepsilon_0\varepsilon_r\nabla^2\psi = F\sum z_i c_i \tag{1}$$

$$\nabla.\overrightarrow{N}_i = \nabla.\left(-D_i\nabla c_i - z_i\frac{D_i}{RT}Fc_i\nabla\psi\right) = 0 \tag{2}$$

In the simulations, electric potential and ionic concentrations inside the representative volume of the mesoporous system are evaluated by solving PNP. PNP equations in 2-D cartesian coordinates are numerically solved by finite element method with COMSOL Multiphysics (www.comsol.com). After a mesh independency study, fine structured mesh was found to be required within and at the inlet/outlet vicinity of the channel, while a coarser triangular mesh structure was adequate for the rest of the domain. In the first iteration, zero electric potential and bulk molar concentrations are assigned on the edges of the domain (shown by dashed lines). Then, the resulting electric potential and ionic distributions developed along the lines ab and cd are used as the boundary condition on the edges of the next iteration. The iteration procedure continues until the defined convergence is reached: The electric potential and ionic concentrations measured at internal center lines (ab and cd) are equal to the ones of assigned at outer center lines.

For the charge regulation to be embedded in the simulations, the protonation/deprotonation reactions occurring on the surface due to the interaction of ions and silanol groups are considered as

$$SiOH \leftrightarrow SiO^- + H^+ \tag{3}$$

$$SiOH + H^+ \leftrightarrow SiOH_2^+ \tag{4}$$

The equilibrium constants of these reactions are calculated by using the site density of the silanol groups (Γ_{SiO^-}, Γ_{SiOH}, and $\Gamma_{SiOH_2^+}$) and the hydrogen concentration at the interface $[H^+]_w$:

$$K_A = \frac{\Gamma_{SiO^-}[H^+]_w}{\Gamma_{SiOH}}, K_B = \frac{\Gamma_{SiOH_2^+}}{\Gamma_{SiOH}[H^+]_w} \tag{5}$$

Using these parameters, the surface charge density, used as a boundary condition on the solid surfaces to model charge regulation nature of silica surfaces, is calculated as

$$\sigma_w = -\frac{F\Gamma_{total}}{N_A}\frac{K_A - K_B[H^+]_w^2}{K_A + [H^+]_w + K_B[H^+]_w^2} \tag{6}$$

For all the simulations, pH, temperature, and the bulk concentration of KCl are kept constant as 6, 300 K, and 0.4 mM, respectively. Total site density (N_{total}) is defined to be 4.816 sites/nm^2 while the equilibrium constants pK_A and pK_B are taken as 7 and 1.9. The diffusivities of H^+, K^+, Cl^-, and OH^- ions are 9.31×10^{-9}, 1.957×10^{-9}, 2.032×10^{-9}, and 5.3×10^{-9} m^2/s, respectively. The following values are used for the constants: $\varepsilon_0\varepsilon_r = 7.08\times10^{-10}$ F/m, $R = 8.31$ J/(mol K), $F = 96{,}485$ C/mol.

The numerical model is validated with the approximate analytical solution for a semi-infinite flat surface proposed by Yeh et al. [56]. The semi-infinite surface condition is preserved by keeping the KCl concentrations at high values (i.e., 10 mM and 100 mM). These high concentrations prevent EDLs of opposite surfaces from overlapping, and the surface charge density can be evaluated using PB. In Fig. 3, the surface charge density values for pH varying from 3 to 9 are depicted. As seen, the current numerical model presented by markers shows an excellent match with the flat surface theory.

Results and discussion

The structural parameters of a mesoporous system (H, ϵ, and R_{pt}) are systemically varied to characterize their effects on the surface charge properties. The pH and KCl concentration are kept constant at 6 and 0.4 mM throughout all simulations. EDL thickness, λ, for these values corresponds to 15 nm and may result in strong EDL overlap depending on the pore size, H. We initiated our study by resolving the electric potential distributions for pore sizes of 50 nm and 100 nm with changing pore to throat size ratios ($R_{pt} = 2.5, 3, 5, 10$) at constant porosity, $\epsilon = 0.5$. Throat size was varied between 5 nm and 20 nm for pore size of 50 nm and between 10 nm and 40 nm for pore size of 100 nm. The domain shown in Fig. 1 is studied while the electric potential contours presented in Fig. 4 is one-fourth of the domain since the remaining parts are symmetry of it. In Fig. 4, each row is at the same pore size with decreasing pore to throat size ratio. A strong EDL overlap is

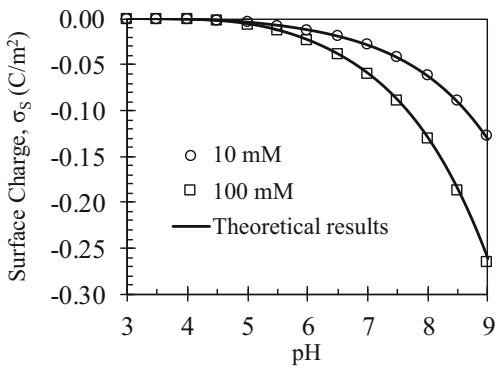

Fig. 3 Validation of the numerical model inside mesoporous silica

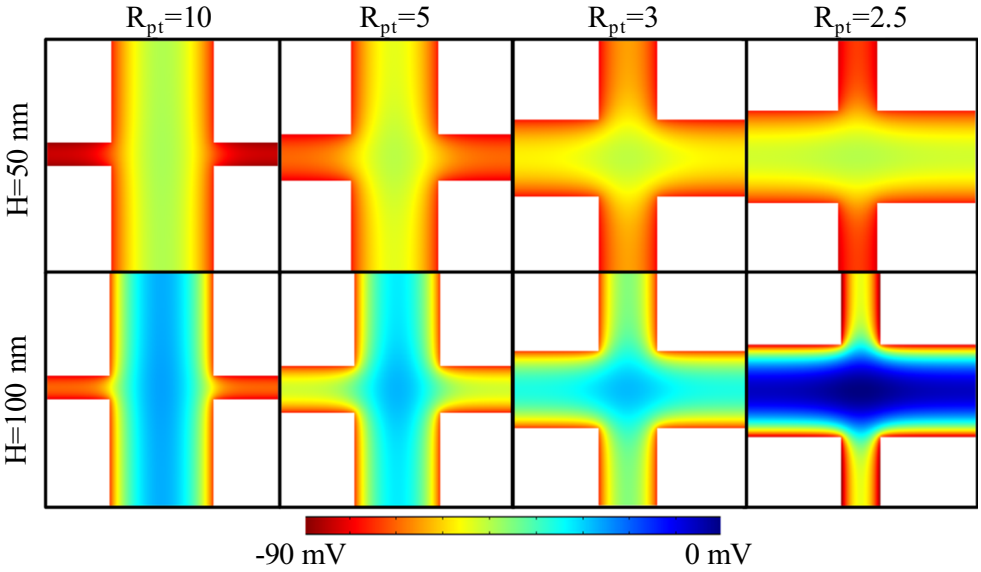

Fig. 4 Electric potential contours for different pore sizes (H) and pore to throat size ratios (R_{pt}) at $\epsilon = 0.5$

clearly distinguished for all the cases in the first row where $H = 50$ nm. Especially for high R_{pt} values, the magnitude of electric potential in the pore throat increases, creating a different ionic environment than the pore center. If the pore size is increased to 100 nm (i.e., second row), the magnitude of electric potential can decrease to zero potential for $R_{pt} = 2.5$ at the pore center, which corresponds to bulk conditions. Keeping in mind that these eight cases are at the same porosity, results prove that the characterization of surface charge density cannot be done solely by porosity.

To further examine the overall and local effects of the pore to throat connectivity, pore size, and corresponding EDL overlap on the surface charging behavior, we plot the local normalized surface charge densities along the pore throats in Fig. 5. Basically, surface charge along the throat surface in both x- and y-direction are given at different pore sizes and pore to throat size ratios while porosity was kept constant at $\epsilon = 0.5$. Decreasing R_{pt} at constant porosity level yields wider pore throats in x-direction while it creates narrower pore throats y-direction. Therefore, an opposite behavior in surface charge variation is expected to be seen in these directions with the change of pore to throat size ratios.

Two distinct mechanisms of local variation can be seen from four different cases ($R_{pt} = 10$, 5, 3, 2.5) presented in Fig. 5. The first mechanism depends on the degree of EDL overlap which decreases the surface charge along the pore throat. The difference between pore sizes 50 nm (solid lines) and 100 nm (dashed lines) is attributed to the varying degree of EDL overlap. With decreasing R_{pt} values, this effect fades away in axial (x-) direction while it becomes dominant in

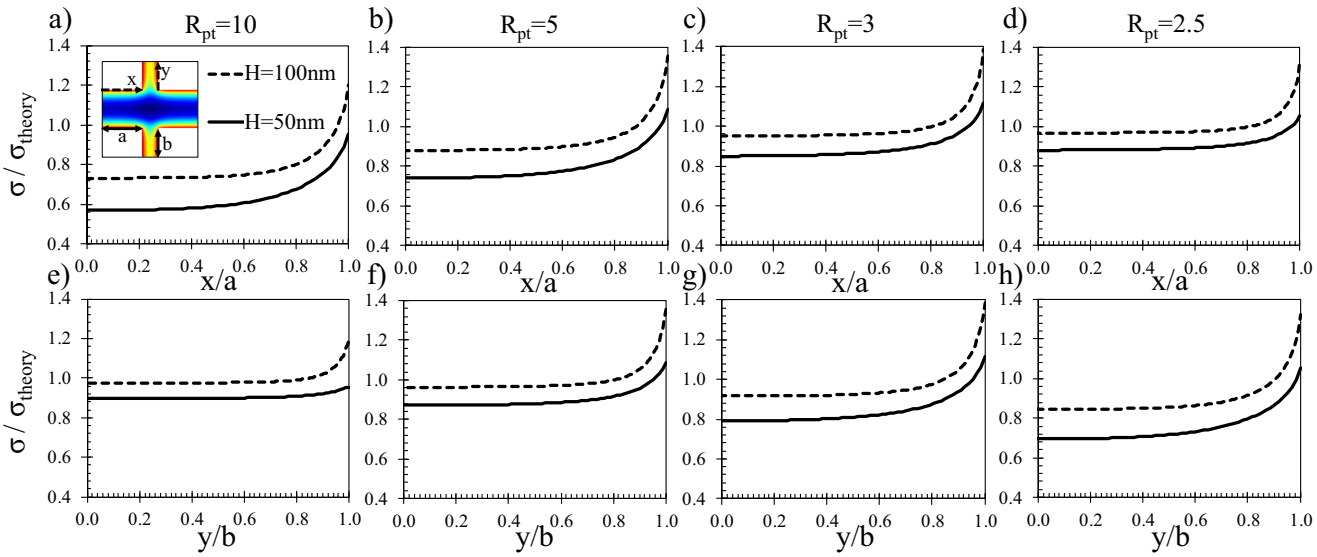

Fig. 5 Normalized surface charge density distribution along the pore throats in the axial direction (x-direction) (**a**, **b**, **c**, **d**) and in the normal direction (y-direction) (**e**, **f**, **g**, **h**) at porosity, $\epsilon = 0.5$

normal (y-) direction. The second mechanism, which is the pore to throat connectivity, increases the magnitude of surface charge density towards the pore void along the pore throats in the axial direction. For high R_{pt} values, the increase is steeper indicating that the effect of connectivity is high. Hence, a longer throat length is required for the connectivity effects to be damped at which the normalized charge density reaches a plateau. For example, while the edge of this plateau is around $x/a = 0.8$ for $R_{pt} = 2.5$, it propagates even into $x = 0.4$ at $R_{pt} = 10$ for the pore throats in axial direction. Another important outcome of Fig. 5 is the trend of overall surface charge density behavior as a function of pore to throat size ratio, R_{pt}. If the first row of Fig. 5a–d is taken into consideration, the average charge density in the pore increases by decreasing R_{pt}, mostly due to the lessening rate of EDL overlap. As the pore throat to pore void connectivity effects weakens with decreasing R_{pt}, charge variation along the throat decreases. Conversely, the opposite can be observed for the second row that presents the result of throats in normal direction.

Once the response of surface charge density to pore to throat size ratio is resolved, we studied these effects at different porosities. In Fig. 6, the average surface charge densities of the pore throat normalized with theoretical estimations are presented as a function of porosity, ϵ, for different R_{pt} and H values. Due to geometrical constraints, there is a limit for maximum R_{pt} value for each pore size. For instance, the maximum value R_{pt} for 50 nm of pore size is 10. For this reason, the pore size is also increased up to 800 nm to reach R_{pt} values up to 200. This way, the R_{pt} range is wide enough to enable proper characterization. Additionally, in order to neglect nano-scale molecular effects, the minimum value for R_{pt} is kept as 1.7 with a minimum throat thickness of 4 nm. While changing the R_{pt} of the system, two successive steps are followed. In the first one, the aspect ratio (AR) of solid parts is kept unity so that the pore throats in both axial and normal directions show identical behavior. This methodology results in only one R_{pt} value that corresponds to a specific porosity level. More detailed analysis of this matter can be found in our other work [30]. However, the main goal of the current study is to examine the dependence of charge density on the R_{pt} and the dependence is strongly related with the interaction of pore throats with the pore volume itself, as discussed in Figs. 4 and 5. Thus, different R_{pt} values at certain porosities are defined as a second step and the elementary volume of mesoporous system is constructed without aspect ratio being unity. In Fig. 6a–d, there are some cases where the results at AR = 1 and different R_{pt} values (where AR ≠ 1) coincide and correspond to the same normalized charge density. This can be attributed to geometrically similar behavior of mesoporous systems for these cases. Figure 6 a shows the variation of the average surface charge density with changing porosity and R_{pt} values for the pore size of 50 nm. At a specific R_{pt}

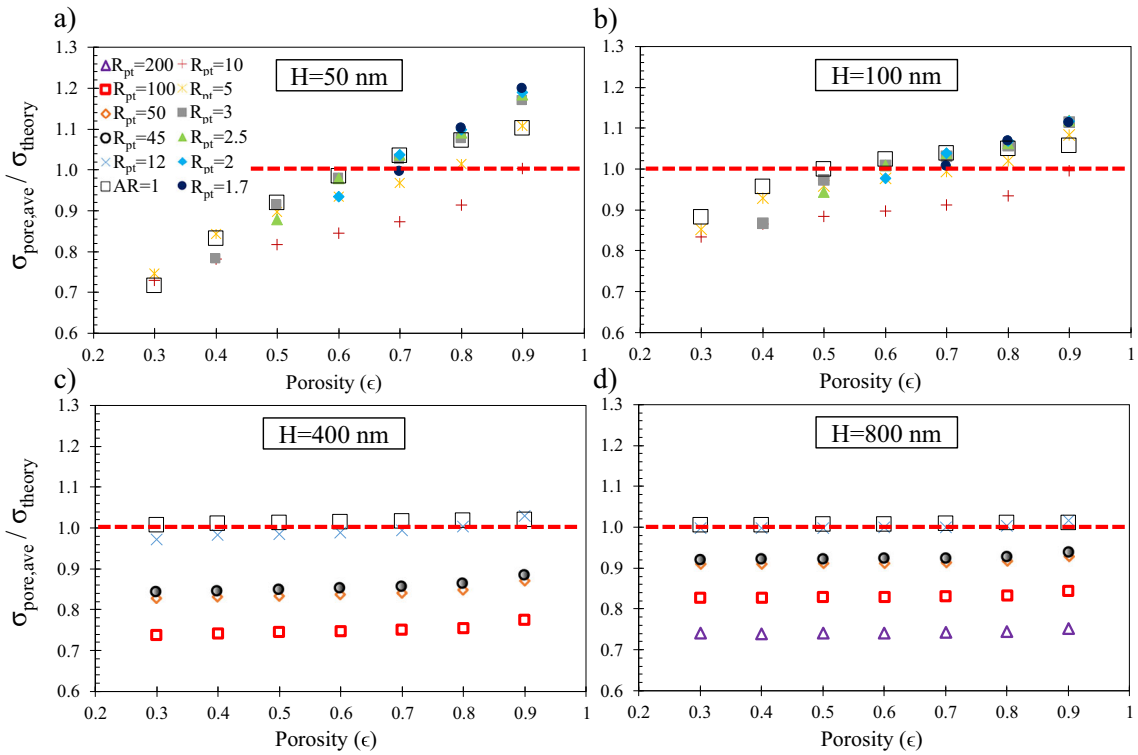

Fig. 6 The averaged surface charge density of mesoporous silica at pore sizes of **a** 50 nm, **b** 100 nm, **c** 400 nm, and **d** 800 nm for different porosity and pore to throat size ratios. Surface charges were normalized by the theoretical calculations for a flat surface at the corresponding ionic conditions. Results of unity aspect ratio systems (AR = 1) for each case are also given

value, the charge density increases with porosity. On the contrary, the charge density decreases by increasing R_{pt} values at a constant porosity. As discussed earlier, the connectivity effects tend to increase the magnitude of charge density. Therefore, there are some cases where the normalized charge density reaches above unity due to strong connectivity effects at high porosities. However, the increase due to porosity decreases as the pore size grows (Fig. 6a–d) and the dependence on R_{pt} becomes stronger. For example, the average charge density of $H = 800$ nm case (Fig. 6d) becomes constant as a function of porosity while the magnitude of normalized average charge decreases by increasing R_{pt}. This is mostly due to the weakening effects of connectivity with the growth of pore size and increasing effects of EDL overlap resulting from the narrower pore throats at higher R_{pt} levels.

Current results showed that the pore connectivity has a dominant effect on internal surface charging. Our earlier work devised a phenomenological model describing internal surface charge as a function of porosity and pore size for the porous systems where the aspect ratio of solid parts in the domain was unity (AR = 1) as ref [30];

$$\frac{\sigma_{\text{pore,ave (AR=1)}}}{\sigma_{\text{theory}}} = 1-\exp\left(-\frac{H\times\varepsilon}{\lambda}\right)+0.3\left(\frac{H}{\lambda\times\varepsilon}\right)^{-0.8} \quad (7)$$

Using the current results, we aim to extend Eq. (7) to include the connectivity effects. All results of different porosity (ϵ), pore size (H), and pore to throat size ratio (R_{pt}) values are summarized in Fig. 7. We normalized these average surface charge densities with the surface charge prediction of Eq. (7) for the corresponding λ/H and ε values. Hence, we can see the deviation from our earlier model by the variation in pore connectivity. As depicted, the normalized charge density as a function of R_{pt} displayed an exponential decay by the increase in R_{pt}. At low R_{pt} values, connectivity effects were negligible that Eq. (7) can provide accurate results. By increasing pore to throat size ratio, average surface charge decreased converging to 75% of the Eq. (7)'s prediction approximately. Even though connectivity effects showed an additional dependence on porosity, we attempted to fit an exponential function onto the overall behavior observed in Fig. 6 as

$$\frac{\sigma_{\text{pore,ave}}}{\sigma_{\text{pore,ave (AR=1)}}} = 0.25e^{-0.02R_{pt}}+0.75 \quad (8)$$

For the small R_{pt} values less than 10 ($R_{pt} < 10$), Eq. (8) yields to unity value representing negligible connectivity effects where Eq. (7) is applicable. On the other hand, for $R_{pt} > 10$ cases, internal mesoporous surface charge decreased by the increasing R_{pt} that Eq. (7) needs to be updated by Eq. (8).

Conclusion

Surface charge density inside mesoporous silica is characterized by systematically changing the porosity, pore size, and pore to throat size ratio. Contrary to existing studies in the literature that focus on the outer charging properties, this study validates the importance of internal surface charge density. The results of 130 different cases prove that any characterization based on porosity and pore size is incomplete to describe the overall behavior of mesoporous systems. In fact, the ratio of pore throat size to pore void size plays a very important role in internal surface charging. Strong EDL overlaps develop in the pore throats for throat sizes comparable with the EDL thickness causing a decrease of absolute value of the surface

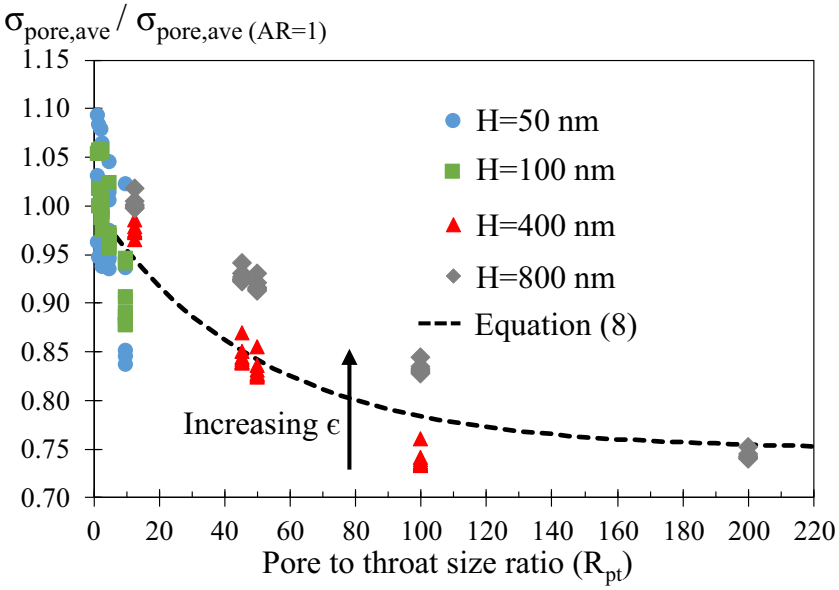

Fig. 7 Average surface charge densities of the mesoporous system (at AR ≠ 1) normalized by the predictions of Eq. (7) for the corresponding porosity, pore size, and ionic condition

charge. Due to EDL overlap, ionic equilibrium inside throats becomes different than ionic condition of pore voids, which develops further variation in surface charge along the axial direction. Such occurrence is the effect of pore connectivity which increases the absolute value of surface charge. For a constant pore size and porosity, both EDL overlap and pore connectivity show variation by the change of throat size. Overall, increase of R_{pt} decreases the absolute magnitude of surface charge. In our earlier work, we formulized internal surface charge as a function of pore size and porosity for the porous systems with aspect ratio of solid parts unity (AR = 1). We extended this model based on current results, in order to consider the pore connectivity effects as a function of pore to throat size ratio (R_{pt}). The extended phenomenological model can predict the average mesoporous internal surface charge as a function of EDL thickness, pore size, porosity, and pore to throat size ratio.

Acknowledgments This work was supported by the Scientific and Technological Research Council of Turkey (TÜBİTAK) under the Grant Number 118M710. Authors also would like to thank the Center for Scientific Computation at Southern Methodist University.

Funding information This work was supported by the Scientific and Technological Research Council of Turkey (TÜBİTAK) under the Grant Number 118M710

Compliance with ethical standards

Conflict of interest The authors declare that they have no conflict of interest.

References

1. Zheng H, Tai CW, Su J, Zou X, Gao F (2015) Ultra-small mesoporous silica nanoparticles as efficient carriers for pH responsive releases of anti-cancer drugs. Dalton Trans 44(46):20186–20192
2. Bharti C, Gulati N, Nagaich U, Pal AK (2015) Mesoporous silica nanoparticles in target drug delivery system: a review. Int J Pharm Investig 5(3):124–133
3. Sancenon F et al (2015) Gated silica mesoporous materials in sensing applications. ChemistryOpen 4(4):418–437
4. Li L-L, Sun H, Fang CJ, Xu J, Jin JY, Yan CH (2007) Optical sensors based on functionalized mesoporous silica SBA-15 for the detection of multianalytes (H+ and Cu2+) in water. J Mater Chem 17(42):4492
5. Kim HJ, Brunelli NA, Brown AJ, Jang KS, Kim WG, Rashidi F, Johnson JR, Koros WJ, Jones CW, Nair S (2014) Silylated mesoporous silica membranes on polymeric hollow fiber supports: synthesis and permeation properties. ACS Appl Mater Interfaces 6(20): 17877–17886
6. Kim H.J., Lim J.E., Shul Y.G., Han H. 2004 Mesoporous silica: polymer composite membrane for direct methanol fuel cell, in Studies in Surface Science and Catalysis . p. 3036–3043
7. Li W, Liu J, Zhao D (2016) Mesoporous materials for energy conversion and storage devices. Nat Rev Mater 1(6)
8. Diagboya PNE, Dikio ED (2018) Silica-based mesoporous materials; emerging designer adsorbents for aqueous pollutants removal and water treatment. Microporous Mesoporous Mater 266:252–267
9. Castillo X, Pizarro J, Ortiz C, Cid H, Flores M, de Canck E, van der Voort P (2018) A cheap mesoporous silica from fly ash as an outstanding adsorbent for sulfate in water. Microporous Mesoporous Mater 272:184–192
10. Jimbo T, Tanioka A, Minoura N (1998) Characterization of an amphoteric-charged layer grafted to the pore surface of a porous membrane. Langmuir 14(25):7112–7118
11. Jimbo T, Higa M, Minoura N, Tanioka A (1998) Surface characterization of poly (acrylonitrile) membranes graft-polymerized with ionic monomers as revealed by ζ potential measurement. Macromolecules 31(4):1277–1284
12. Peeters JMM, Mulder MHV, Strathmann H (1999) Streaming potential measurements as a characterization method for nanofiltration membranes. Colloids Surf A Physicochem Eng Asp 150(1–3):247–259
13. Datta S, Conlisk AT, Kanani DM, Zydney AL, Fissell WH, Roy S (2010) Characterizing the surface charge of synthetic nanomembranes by the streaming potential method. J Colloid Interface Sci 348(1):85–95
14. Afonso M (2001) Streaming potential measurements to assess the variation of nanofiltration membranes surface charge with the concentration of salt solutions. Sep Purif Technol 22-23(1–2):529–541
15. Dimos K, Stathi P, Karakassides MA, Deligiannakis Y (2009) Synthesis and characterization of hybrid MCM-41 materials for heavy metal adsorption. Microporous Mesoporous Mater 126(1–2):65–71
16. Dove PM, Craven CM (2005) Surface charge density on silica in alkali and alkaline earth chloride electrolyte solutions. Geochim Cosmochim Acta 69(21):4963–4970
17. Salis A, Parsons DF, Boström M, Medda L, Barse B, Ninham BW, Monduzzi M (2010) Ion specific surface charge density of SBA-15 mesoporous silica. Langmuir 26(4):2484–2490
18. Martínez Casillas DC, Longinotti MP, Bruno MM, Vaca Chávez F, Acosta RH, Corti HR (2018) Diffusion of water and electrolytes in mesoporous silica with a wide range of pore sizes. J Phys Chem C 122(6):3638–3647
19. Rho H, Chon K, Cho J (2018) Surface charge characterization of nanofiltration membranes by potentiometric titrations and electrophoresis: functionality vs. zeta potential. Desalination 427:19–26
20. Goyne KW, Zimmerman AR, Newalkar BL, Komarneni S, Brantley SL, Chorover J (2002) Surface charge of variable porosity Al2O3(s) and SiO2(s) adsorbents. J Porous Mater 9(4):243–256
21. Lan W-J, Holden DA, Liu J, White HS (2011) Pressure-driven nanoparticle transport across glass membranes containing a conical-shaped nanopore. J Phys Chem C 115(38):18445–18452
22. Bowen WR, Hughes DT (1991) Properties of microfiltration membranes: the surface electrochemistry of anodic film membranes. J Colloid Interface Sci 143(1):252–265
23. Huang K, Yang R (2007) Electrokinetic behaviour of overlapped electric double layers in nanofluidic channels. Nanotechnology 18: 115701
24. B. J. Kirby 2010 Micro-nanoscale fluid mechanics transport in microfluidic devices, Cornell University, New York
25. Hung S.W., C.P. Chen, and C.C. Chieng 2008. *Ionic transport in finite length nano-sized pores and channels*. in *ASME First International Conference on Micro/Nanoscale Heat Transfer*. 2008. Tainan
26. Lin CY, Yeh LH, Siwy ZS (2018) Voltage-induced modulation of ionic concentrations and ion current rectification in mesopores with highly charged pore walls. J Phys Chem Lett 9(2):393–398
27. Mao M, Ghosal S, Hu G (2013) Hydrodynamic flow in the vicinity of a nanopore induced by an applied voltage. Nanotechnology 24(24):245202

28. Hsu J-P, Lin SC, Lin CY, Tseng S (2017) Power generation by a pH-regulated conical nanopore through reverse electrodialysis. J Power Sources 366:169–177
29. Lin JY, Lin CY, Hsu JP, Tseng S (2016) Ionic current rectification in a pH-tunable polyelectrolyte brushes functionalized conical nanopore: effect of salt gradient. Anal Chem 88(2):1176–1187
30. Ninham BW, Parsegian VA (1971) Electrostatic potential between surfaces bearing ionizable groups in ionic equilibrium with physiologic saline solution. J Theor Biol 31(3):405–428
31. Sen T, Barisik M (2018) Size dependent surface charge properties of silica nano-channels: double layer overlap and inlet/outlet effects. Phys Chem Chem Phys 20(24):16719–16728
32. Sen T, Barisik M (2019) Internal surface electric charge characterization of mesoporous silica. Sci Rep 9(1):137
33. Le Ravalec M et al (1996) Transport properties and microstructural characteristics of a thermally cracked mylonite. Pure Appl Geophys 146(2):207–227
34. Nelson PH (2009) Pore-throat sizes in sandstones, tight sandstones, and shales. AAPG Bull 93(3):329–340
35. Song Y-Q (2001) Pore sizes and pore connectivity in rocks using the effect of internal field. Magn Reson Imaging 19(3–4):417–421
36. Ioannidis MA, Chatzis I (1993) Network modelling of pore structure and transport properties of porous media. Chem Eng Sci 48(5): 951–972
37. Lindquist WB, Venkatarangan A, Dunsmuir J, Wong TF (2000) Pore and throat size distributions measured from synchrotron X-ray tomographic images of Fontainebleau sandstones. J Geophys Res Solid Earth 105(B9):21509–21527
38. Barisik M, Atalay S, Beskok A, Qian S (2014) Size dependent surface charge properties of silica nanoparticles. J Phys Chem C 118(4):1836–1842
39. Atalay S, Barisik M, Beskok A, Qian S (2014) Surface charge of a nanoparticle interacting with a flat substrate. J Phys Chem C 118(20):10927–10935
40. Beck JS, Vartuli JC, Roth WJ, Leonowicz ME, Kresge CT, Schmitt KD, Chu CTW, Olson DH, Sheppard EW, McCullen SB, Higgins JB, Schlenker JL (1992) A new family of mesoporous molecular sieves prepared with liquid crystal templates. J Am Chem Soc 114(27):10834–10843
41. Kresge CT, Leonowicz ME, Roth WJ, Vartuli JC, Beck JS (1992) Ordered mesoporous molecular sieves synthesized by a liquid-crystal template mechanism. Nature 359(6397):710–712
42. Kleitz F, Choi SH, Ryoo R (2003) Cubic Ia 3 d large mesoporous silica: synthesis and replication to platinum nanowires, carbon nanorods and carbon nanotubes. Chem Commun 17:2136–2137
43. Kleitz F., S. Hei Choi, and R. Ryoo 2003 Cubic Ia3d large mesoporous silica: synthesis and replication to platinum nanowires, carbon nanorods and carbon nanotubes Electronic supplementary information (ESI) available: TEM images of mesoporous cubic silica and Pt networks, XRD patterns during formation of the cubic phase Chemical Communications, (17)
44. Zhao D, Huo Q, Feng J, Chmelka BF, Stucky GD (1998) Nonionic triblock and star diblock copolymer and oligomeric surfactant syntheses of highly ordered, hydrothermally stable, mesoporous silica structures. J Am Chem Soc 120(24):6024–6036
45. Zhao D et al (1998) Triblock copolymer syntheses of mesoporous silica with periodic 50 to 300 angstrom pores. Science 279(5350): 548–552
46. Yu C, Yu Y, Zhao D (2000) Highly ordered large caged cubic mesoporous silica structures templated by triblock PEO–PBO–PEO copolymer. Chem Commun (7):575–576
47. Kim T-W, Ryoo R, Kruk M, Gierszal KP, Jaroniec M, Kamiya S, Terasaki O (2004) Tailoring the pore structure of SBA-16 silica molecular sieve through the use of copolymer blends and control of synthesis temperature and time. J Phys Chem B 108(31):11480–11489
48. Sakamoto Y, Kaneda M, Terasaki O, Zhao DY, Kim JM, Stucky G, Shin HJ, Ryoo R (2000) Direct imaging of the pores and cages of three-dimensional mesoporous materials. Nature 408(6811): 449–453
49. dos Santos SML, Nogueira KAB, de Souza Gama M, Lima JDF, da Silva Júnior IJ, de Azevedo DCS (2013) Synthesis and characterization of ordered mesoporous silica (SBA-15 and SBA-16) for adsorption of biomolecules. Microporous Mesoporous Mater 180: 284–292
50. Narayan R, Nayak U, Raichur A, Garg S (2018) Mesoporous silica nanoparticles: a comprehensive review on synthesis and recent advances. Pharmaceutics 10(3)
51. Knezevic N et al (2018) Hard template synthesis of nanomaterials based on mesoporous silica. Metall Mater Eng 24(4)
52. Gobin O.C. 2006 *SBA-16 materials synthesis, diffusion and sorption properties*. , Laval University. p. 73
53. Brakke KA (1992) The surface evolver. Exp Math 1(2):141–165
54. Zhao H, Zhai S (2013) The influence of dielectric decrement on electrokinetics. J Fluid Mech 724:69–94
55. Wernersson E, Kjellander R (2006) On the effect of image charges and ion-wall dispersion forces on electric double layer interactions. J Chem Phys 125(15):154702
56. Yeh L-H, Xue S, Joo SW, Qian S, Hsu JP (2012) Field effect control of surface charge property and electroosmotic flow in nanofluidics. J Phys Chem C 116(6):4209–4216